Copyright ©2025 by Alban Beshaj. Published by the IAF, with permission and released to the IAF to publish in all forms.

IAC-25-C1,6,5,x102487

Robust guidance for surface characterization of minor bodies

Alban Beshaj[a]*, Antonio Rizza[b], Carmine Giordano[c], Francesco Topputo[d]

[a] *Department of Aerospace Science and Technology, Politecnico di Milano, via La Masa, 34, Milan, 20156, Italy* E-mail: alban.beshaj@polimi.it

[b] *Aeronautics and Astronautics, Stanford University, 496 Lomita Mall, Stanford, CA 94305* E-mail: arizza@stanford.edu

[c] *Department of Aerospace Science and Technology, Politecnico di Milano, via La Masa, 34, Milan, 20156, Italy* E-mail: carmine.giordano@polimi.it

[d] *Department of Aerospace Science and Technology, Politecnico di Milano, via La Masa, 34, Milan, 20156, Italy* E-mail: francesco.topputo@polimi.it

* Corresponding author

Abstract

In recent years, interest in exploring minor bodies has increased significantly. Studying these objects is important for planetary defense against potential impacts and for the valuable scientific and economic opportunities they offer. However, despite their high relevance, minor bodies exploration is dampened by the challenges arising when operating a spacecraft in their close-proximity environment. This work proposes an efficient two-step methodology for generating robust inspection trajectories for surface mapping using impulsive guidance. In the first step, a computationally efficient sampling-based method is used to solve a deterministic optimization problem, which maximizes the scientific return of the trajectory, modeled as the observation of surface regions under specific observation requirements. The output of this stage is provided to the trajectory refinement step, which ensures robustness under the considered trajectory and minimizes fuel consumption. The methodology is tested numerically for Close-Proximity Operations (CPO) around asteroid Itokawa. The results demonstrate the effectiveness of the developed guidance in achieving the objective of surface characterization.

1. Introduction

Minor bodies exploration has recently gained high relevance in the space sector. The reasons underlying this interest are different [1]. Although partial data can be retrieved from Earth-based observations [2], an in-depth characterisation requires close-range measurement. Therefore, space missions capable of operating in close-proximity of the minor body are needed to perform in-situ sensing. Operating in this range poses important challenges: the spacecraft is exposed to a complex and uncertain environment that leaves no margin for communication delays typical of deep-space missions. Consequently, robust and efficient methodologies are required to increase the level of autonomy of this class of space missions, in order to enable a broader exploration of these resourceful space objects.

In this context, particularly relevant are guidance algorithms that must be able to generate trajectories that satisfy both scientific goals, such as surface characterization, and engineering requirements imposed by the system. Multiple works have tackled the problem using different methodologies and focusing on different phases of minor body missions. In [3], both the approach and the close-proximity phases are considered. Specifically, for the second phase, a robust closed-loop control algorithm is proposed to perform station-keeping of a Terminator Orbit (TO). Different approaches [4–6] have formulated the guidance surface mapping problem as a partially observable Markov decision process (POMDP) and solved it with deep reinforcement learning techniques. Closer to this work, in [7–9], both impulsive and continuous CPO guidance are formulated as a goal-oriented problem. In this framework, the surface mapping objectives are formulated as geometric regions evolving around the body. One specific requirement is considered satisfied when the spacecraft spends a certain amount of time inside the associated region. Other studies [10, 11] have focused on enhancing the robustness of trajectories with respect to uncertainties in the same framework.

Copyright ©2025 by Alban Beshaj. Published by the IAF, with permission and released to the IAF to publish in all forms.

Formulating the problem in the framework of goal-oriented trajectory design, this work develops a two-step guidance methodology. The first stage provides a trajectory that maximizes the scientific return in a specific control horizon, and the second refines the trajectory generated in the first step to ensure robustness with respect to uncertainties. The main contributions of this study are:

- The development of a computationally efficient sampling-based method for impulsive goal-oriented guidance around minor bodies.
- The formulation of a trajectory refinement scheme as a chance-constrained convex optimization problem, which ensures robustness with respect to uncertainties with prescribed risk levels.

The paper is structured as follows. In Section 2, the approaches used to model the problem, the dynamics, and the uncertainties considered in the work are presented. Section 3 reports the general formulation of the problem tackled in this study and its decomposition into simpler subproblems. In Section 4, the problems presented in the previous sections are reformulated, and the methodologies used to solve them are described. The paper concludes with Sections 5 and 6, where numerical results and conclusions are reported.

2. Background

The problem tackled in this work is the goal-oriented trajectory design problem [9]. It is particularly relevant for minor body exploration, as it provides a well-suited mathematical description of the typical requirements that characterize this mission class. Indeed, in this context, besides classical engineering requirements associated with operations or fuel consumption minimization constraints, scientific requirements, such as observing specific regions on the asteroid surface, play a crucial role as they are inherently linked to the typical objectives of this class of missions.

This study will utilize the effective modeling approach already established in previous works [7, 8] to model a surface mapping objective through a passive sensor, such as a camera. Specifically, given a set of surface features to be observed, Regions Of Interest (ROI) around the target body are defined based on observation geometry requirements. The key parameters are the emission angle ϵ and incidence angle i, which determine the quality of topography and albedo characterization [4], and the range ρ, which affects the Ground Sampling Distance (GSD) [12]. Mathematically, these three parameters can be expressed as follows:

$$\rho_f({}^{\mathcal{B}}\mathbf{r}) = \left\|{}^{\mathcal{B}}\mathbf{r} - {}^{\mathcal{B}}\mathbf{r}_f\right\|, \tag{1a}$$

$$\epsilon_f({}^{\mathcal{B}}\mathbf{r}) = \arccos\left(\frac{\left({}^{\mathcal{B}}\mathbf{n}_f\right)^\top\left({}^{\mathcal{B}}\mathbf{r} - {}^{\mathcal{B}}\mathbf{r}_f\right)}{\left\|{}^{\mathcal{B}}\mathbf{r} - {}^{\mathcal{B}}\mathbf{r}_f\right\|}\right), \tag{1b}$$

$$i_f(t, {}^{\mathcal{B}}\mathbf{r}) = \arccos\left(\frac{\left({}^{\mathcal{B}}\mathbf{n}_f\right)^\top\left({}^{\mathcal{B}}\mathbf{r}_s(t) - {}^{\mathcal{B}}\mathbf{r}_f\right)}{\left\|{}^{\mathcal{B}}\mathbf{r}_s(t) - {}^{\mathcal{B}}\mathbf{r}_f\right\|}\right). \tag{1c}$$

where ${}^{\mathcal{B}}\mathbf{r}$ is the observer position, ${}^{\mathcal{B}}\mathbf{r}_f$ and ${}^{\mathcal{B}}\mathbf{n}_f$ are the position and the outward surface normal of the feature f, ${}^{\mathcal{B}}\mathbf{r}_s(t)$ represents the Sun position at time t; the left superscript represents the frame where the vectors are expressed, in this case the body frame $\mathcal{B}$. Given a feature and the three geometrical parameters, an ROI can be described as:

$$\mathcal{R}_f(t) = \{\, {}^{\mathcal{B}}\mathbf{r} \in \mathbb{R}^3 \mid \rho_f \in [\rho_f^-, \rho_f^+],\ \epsilon_f \in [\epsilon_f^-, \epsilon_f^+], \\ i_f(t) \in [i_f^-, i_f^+] \,\} \tag{2}$$

where $\rho_{\min}$, $i_{\min}$, $\epsilon_{\min}$ and $\rho_{\max}$, $i_{\max}$, $\epsilon_{\max}$ represent respectively the upper and lower bounds of each parameter that determine the validity of the feature observation. In Figure 1, a simplified representation of an ROI is reported. Note that the ROI can also be expressed in the inertial frame $\mathcal{I}$; however, in this case, additional time dependencies appear in Eq. (2), as the features rotate with the body. The mission objective considered in this study involves passing through multiple ROIs, which constitute the feature set $\mathcal{F}$.

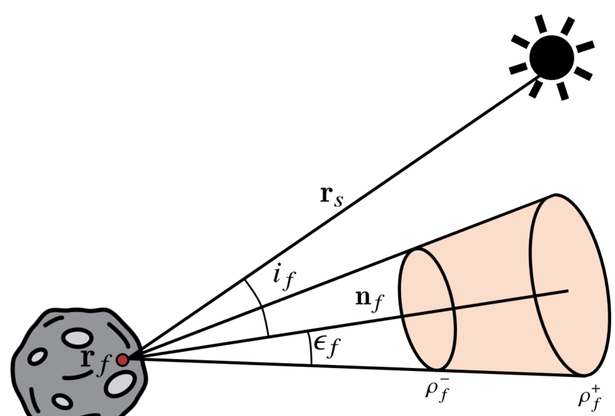

Fig. 1: Simplified ROI representation, ignoring incidence angle dependence.

2.1 Dynamical environment

The orbital dynamics considered includes the typical forces relevant for the motion during CPO around a minor

Copyright ©2025 by Alban Beshaj. Published by the IAF, with permission and released to the IAF to publish in all forms.

body. The general form expressed in the inertial frame $\mathcal{I}$ is:

$$\dot{\mathbf{x}} = \mathbf{f}_f(\mathbf{x}, t) + \mathrm{B} \sum_{i=1}^{N_m} \delta(t - t_i)\, \boldsymbol{\Delta}\mathbf{v_i}. \tag{3}$$

where $\mathbf{x} = [\mathbf{r}^\top,\ \mathbf{v}^\top]^\top$ is the state vector containing the position and velocity of the spacecraft, $\mathbf{f}_f(\mathbf{x}, t)$ represents the free dynamics, and the second term of the right-hand side is associated with the control, considered as impulsive in this work. B is the constant control matrix, $\delta(\cdot)$ is the Dirac function, and $\boldsymbol{\Delta}\mathbf{v_i}$ is the generic impulse executed at time t_i. The free dynamics includes the main accelerations acting on the spacecraft:

$$\begin{aligned}\mathbf{f}_f(\mathbf{x}, t) = \mathbf{f}_g(\mathbf{r}, t) - & \underbrace{\sum_{k \in \mathcal{P}} \mu_k \left(\frac{\mathbf{r}_k}{\|\mathbf{r}_k\|^3} + \frac{\mathbf{r} - \mathbf{r}_k}{\|\mathbf{r} - \mathbf{r}_k\|^3} \right)}_{\text{3-body acc.}} \\ & + \underbrace{C_r \frac{A}{m} \frac{P_0 d_0^2}{c} \frac{\mathbf{r} - \mathbf{r}_s}{\|\mathbf{r} - \mathbf{r}_s\|^3}}_{\text{SRP}}.\end{aligned} \tag{4}$$

where $\mathbf{r}$ is the spacecraft position in the inertial frame, μ_k, r_k are respectively the gravitational parameter and the position of the generic body part of the set of third perturbing bodies $\mathcal{P}$. The solar radiation pressure, computed through the cannonball model, is defined by the reflectivity coefficient C_r, the effective area and mass of the spacecraft A and m, the solar flux at the distance of 1 Astronomical Unit (AU) P_0, the Sun-Earth distance at 1 AU d_0, the speed of light c, and the Sun position $\mathbf{r}_s$.

The contribution given by the term $\mathbf{f}_g(\mathbf{r}, t)$ represents the gravitational attraction of the minor body, which can be expressed as:

$$\mathbf{f}_g(\mathbf{r}, t) = [\mathcal{I}\mathcal{B}]\ \nabla U \tag{5}$$

where $[\mathcal{I}\mathcal{B}]$ is the rotation matrix from the body frame $\mathcal{B}$ to the intertial frame $\mathcal{I}$. U is the gravitational potential, which is approximated through a truncated spherical expansion [13]:

$$\begin{aligned}U(r, \phi, \lambda) = \frac{\mu}{r} + \frac{\mu}{r} \Big[\sum_{n=2}^{N} \sum_{m=0}^{n} \left(\frac{R}{r}\right)^n \bar{P}_{n,m}(\sin\phi) \\ \times \big(\bar{C}_{n,m} \cos(m\lambda) + \bar{S}_{n,m} \sin(m\lambda)\big) \Big].\end{aligned} \tag{6}$$

where μ is the gravitational parameter of the body, R is the reference radius, (r, ϕ, λ) are the spherical coordinates of the spacecraft position in body frame, N is the truncation order. $\bar{P}_{n,m}[x]$ is the associated normalized Legendre function of order n and degree m, and $\bar{C}_{n,m}$ and $\bar{S}_{n,m}$ are the normalized potential coefficients.

In addition to the nominal dynamics, the evolution of perturbed initial conditions around the nominal one is also relevant in the context of this work. In this context, a first-order expansion of the nominal dynamics is used. Under this approximation, the perturbation dynamics can be described by the following linear equation:

$$\delta\mathbf{x}(t) = \Phi(t, t_0)\, \boldsymbol{\delta}\mathbf{x}_0 + \sum_{i=1}^{N_m} \Phi(t, t_i)\, \mathrm{B}\, \boldsymbol{\delta}\mathbf{v_i} \tag{7}$$

where $\boldsymbol{\delta}\mathbf{x}_0$ is the initial perturbation at time t_0, N_m is the total number of maneuvers in the time interval $[t_0,\ t]$, and $\boldsymbol{\delta}\mathbf{v}_\mathrm{i}$ is a maneuver at t_i, sufficiently small to avoid compromising the first-order approximation. $\boldsymbol{\Phi}$ is the State Transition Matrix (STM), whose dynamics is governed by:

$$\dot{\Phi}(t, t_0) = \left.\frac{\partial \mathbf{f}_f}{\partial \mathbf{x}}\right|_{\hat{\mathbf{x}}} \Phi(t, t_0). \tag{8}$$

where $\hat{\mathbf{x}}$ is the nominal trajectory around which the expansion is performed. To obtain the STM evolution, Eq. (8) is propagated with the nominal state. The Jacobian of the nominal dynamics, required for STM propagation, is evaluated analytically for each modeled perturbation.

2.2 Uncertainties

Different types of uncertainties characterize minor body missions. Primarily, they are related to navigation, control execution errors, and dynamics. Considering the state variable as deterministic is limiting; a probabilistic representation is required. In this work, the state will be approximated through a Gaussian distribution that will be propagated linearly. This choice simplifies the mathematical formulation of the guidance problem and enhances the computational efficiency. Moreover, it is justified by the limited planning horizon that will be considered, as well as the fact that the spacecraft will operate sufficiently far from the body, thereby limiting interaction with the complex dynamics in the region close to the surface. In this way, the errors associated with the conservative nature of linear covariance propagation will be limited.

Given an initial state described by $\mathbf{x_0} = \mathcal{N}(\bar{\mathbf{x}}(\mathbf{t_0}), P_0)$, using a LinCov method, the evolution of the state covariance is provided by [14]:

$$P(t) = \begin{bmatrix} P_{rr} & P_{rv} \\ P_{vr} & P_{vv} \end{bmatrix} = \Phi(t, t_0)\ P_0\ \Phi(t, t_0)^\mathrm{T} \tag{9}$$

where P_0 represents the Gaussian distribution at initial time t_0.

Copyright ©2025 by Alban Beshaj. Published by the IAF, with permission and released to the IAF to publish in all forms.

Eq. (9) represents the free evolution of the state distribution governed by the dynamics in Eq. (3). However, the effect of control uncertainties in the control execution is not considered. In order to take into account this aspect, the Gates model is used [15]. The model consists of impulsively updating the state covariance after the execution of an impulse. Given the magnitude error standard deviations σ_m, and the pointing error standard deviation σ_p, the bottom left 3x3 submatrix of state distribution $P(t_i)$ at the maneuver time t_i can be updated by adding the following contribution [16]:

$$P_{\Delta v}(\Delta \mathbf{v}_i) = \sigma_m^2 \, \Delta \mathbf{v}_i \, \Delta \mathbf{v}_i^\top + \sigma_p^2 \left[\Delta \mathbf{v}_i \times\right]\left[\Delta \mathbf{v}_i \times\right]^\top . \quad (10)$$

where $\left[\Delta \mathbf{v}_i \times\right]$ is the skew-symmetric matrix constructed with the impulse vector $\Delta \mathbf{v}_i$.

3. Problem formulation

As anticipated, missions to minor bodies impose different types of requirements. Before delving deeper into the formulation of the problem, the details associated with the main requirements relevant to the analyzed scenario will be expressed in mathematical form, allowing them to be incorporated as constraints or objectives in the formulation of the guidance optimization problem.

3.1 Scientific requirements

Building on the scientific requirements introduced in Section 2, a potential function is introduced to quantify the satisfaction of the conditions of a specific region $\mathcal{R}_f$. Following the formulation given in [12], the following continuous function can be used:

$$\omega_f(\mathbf{y}_\mathrm{f}) = \mathcal{D}_f\big(y_{f,1}\big) \cdot \mathcal{E}_f\big(y_{f,2}\big) \cdot \mathcal{I}_f\big(y_{f,3}\big). \quad (11)$$

where

$$\mathbf{y}_\mathrm{f}(\mathbf{r}, t) = \begin{bmatrix} y_{f,1} \\ y_{f,2} \\ y_{f,3} \end{bmatrix} = \begin{bmatrix} \rho_f(\mathbf{r}) \\ \epsilon_f(\mathbf{r}) \\ i_f(t, \mathbf{r}) \end{bmatrix}. \quad (12)$$

The functions $\mathcal{D}_f$, $\mathcal{E}_f$, and $\mathcal{I}_f$ are sigmoid functions:

$$\mathcal{D}_f\big(y_{f,1}\big) = \frac{1}{1 + e^{-K_1\left(y_{f,1} - \left(\frac{\rho_f^-}{\bar{R}}\right)^2\right)}} \cdot \frac{1}{1 + e^{K_1\left(y_{f,1} - \left(\frac{\rho_f^+}{\bar{R}}\right)^2\right)}},$$
$$\mathcal{E}_f\big(y_{f,2}\big) = \frac{1}{1 + e^{-K_2\left(y_{f,2} - \cos\epsilon_f^+\right)}},$$
$$\mathcal{I}_f\big(y_{f,3}\big) = \frac{1}{1 + e^{-K_3\left(y_{f,3} - \cos i_f^+\right)}}. \quad (13)$$

where K_1, K_2, K_3 are parameters that define the shape of the sigmoid functions, $\bar{R}$ is the reference distance from the body, used to normalize the range.

Given the above functions, in a time interval $[t_0,\ T_h]$ the time spent in the specific $\mathcal{R}_f$ can be expressed as:

$$T_f = \int_{t_0}^{T_h} \omega_f(\mathbf{y}_\mathrm{f}) \, d\tau \quad (14)$$

3.2 Engineering requirements

In addition to scientific requirements, several engineering constraints must be respected. First of all, the state shall evolve within a safe operating envelope, defined by the following set:

$$\mathcal{X} = \{\mathbf{r} \in \mathbb{R}^3 \mid \ R_{imp} \leq \ \|\mathbf{r}\| \leq R_{esc}\} \quad (15)$$

where R_{imp} and R_{esc} represent the upper and lower bounds in terms of distance from the center of the body, respectively. Typically, R_{imp} is chosen equal to the maximum dimension of the body plus a safety margin to mitigate impact risk under uncertainties. On the other hand, R_{esc} is selected to minimize the probability of escape, thus keeping the spacecraft in gravity-dominated regions, where it can be recovered in case of missed maneuver events. Other engineering constraints are related to the spacecraft propulsion capabilities. Given the limited authority of the thrusters, the impulse magnitude must be bounded. Therefore, the set of admissible control actions is:

$$\mathcal{U} = \{\Delta\mathbf{v} \in \mathbb{R}^3 \mid \ \|\Delta\mathbf{v}\| \leq \Delta v_{max}\} \quad (16)$$

where Δv_{max} is the maximum impulse that can be provided by the system.

In the context of control action, an additional operational constraint imposes a minimum time separation ΔT_m between consecutive maneuvers. Frequent control actions must be avoided for different reasons. First, maneuvers close in time can be demanding from a system point of view. Moreover, degradation in the navigation solution can be experienced: measurements are unavailable during thrusting, and the navigation solution requires time to converge after the introduction of a discontinuity in the state. Therefore, executing frequent maneuvers can yield suboptimal guidance solution given the poor state knowledge used to compute it.

3.3 Guidance problem

Provided the constraint and objective formulations described above, a guidance problem for the surface characterization of the minor body can be formulated. The

Copyright ©2025 by Alban Beshaj. Published by the IAF, with permission and released to the IAF to publish in all forms.

problem is posed as an optimal control problem whose objective is to minimize the time t_f required to complete the surface characterization, which consists of observing each feature of the feature set $\mathcal{F}$ for at least a time instant t_k, without violating the operational constraints throughout the trajectory. The formal statement is given in Eq. (17), where $\mathbf{t_m} = [t_1, \ldots, t_{N_m}]^\top$ and $\Delta\mathbf{v}_m = \left[\, \Delta\mathbf{v}_1^\top \; \cdots \; \Delta\mathbf{v}_{N_m}^\top \,\right]^\top$ are N_m x 1 and (3 x N_m) x 1 vectors containing the maneuver times and impulses, $\mathbf{t_{k,tot}}$ is a N_f x 1 vector containing the t_k that satisfies Eq. (17h) for each considered feature.

$$
\begin{aligned}
&\underset{t_f,\, \mathbf{t}_\mathrm{m},\, \Delta\mathbf{v}_\mathrm{m},\, \mathbf{t}_\mathrm{k,tot}}{\text{minimize}} \quad t_f && && \text{(17a)}\\
&\text{subject to} \\
&\text{Eq. (3)} && \forall\, t \in [t_0, t_f], && \text{(17b)}\\
&\mathbf{x}(t_0) = \mathbf{x}_0, && && \text{(17c)}\\
&\mathbf{x}(t) \in \mathcal{X} && \forall\, t \in [t_0, t_f], && \text{(17d)}\\
&\Delta\mathbf{v}_i \in \mathcal{U} && \text{for } i = 1, \ldots, N_m, && \text{(17e)}\\
&t_0 \le t_1 \le \cdots \le t_{N_m} \le t_f, && && \text{(17f)}\\
&t_i - t_{i-1} \ge \Delta T_\mathrm{m} && \text{for } i = 2, \ldots, N_m, && \text{(17g)}\\
&\mathbf{x}(t_k) \in \mathcal{R}_f \text{ for } t_k \in [t_0, t_f] && \forall\, f \in \mathcal{F}. && \text{(17h)}
\end{aligned}
$$

The high dimensionality of this optimization problem poses significant limitations in solving it onboard. Moreover, the large dispersion caused by uncertainties makes the open-loop solution of Eq. (17) unreliable. For these reasons, in this study, the problem is simplified to increase tractability from a computational perspective, at the expense of optimality. First, the planning horizon is reduced from the full mission time t_f to a shorter horizon T_h. Second, the new planning horizon $[t_0,\ T_h]$ admits only one impulse, whose value is obtained by solving two simpler problems in sequence.

The first subproblem, which will be referred to as the trajectory generation problem, seeks the single impulse $\Delta\mathbf{v_i}$ at time t_i that maximizes the time spent inside the ROIs over the time interval $[t_i,\ t_{i+1}]$. To enhance computational efficiency, the state variable is considered deterministic. Formally, the trajectory generation problem is stated in Eq. (18), where ΔT_p represents a time window that constrains the next maneuver time.

The solution of the trajectory generation problem, solved with the method described in Subsection 4.1, yields a trajectory evolving in the time interval $[t_0,\ t_{i+1}]$ that crosses a subset of features $\mathcal{F}_g \subseteq \mathcal{F}$. This trajectory is provided as an initial guess for a second problem, i.e., the trajectory refinement problem, which considers the state as a distribution and provides a trajectory that is robust with respect to the considered uncertainties.

$$
\begin{aligned}
&\underset{t_i,\, t_{i+1},\, \Delta\mathbf{v}_i}{\text{maximize}} \quad \sum_{f=1}^{N_f} T_f && && \text{(18a)}\\
&\text{subject to} \\
&\text{Eq. (3)} && \forall\, t \in [t_0, t_{i+1}], && \text{(18b)}\\
&\mathbf{x}(t_0) = \mathbf{x}_0, && && \text{(18c)}\\
&\mathbf{x}(t) \in \mathcal{X} && \forall\, t \in [t_0, t_{i+1}], && \text{(18d)}\\
&\Delta\mathbf{v}_i \in \mathcal{U}, && && \text{(18e)}\\
&t_i \in [t_0,\ t_0 + \Delta T_p] && && \text{(18f)}\\
&t_{i+1} \in [t_i + \Delta T_m,\ t_i + \Delta T_m + \Delta T_p]. && && \text{(18g)}
\end{aligned}
$$

The trajectory refinement problem is formulated as follows:

$$
\begin{aligned}
&\underset{\Delta\mathbf{v}_i}{\text{minimize}} \quad \|\Delta\mathbf{v}_i\| && && \text{(19a)}\\
&\text{subject to} \\
&\text{Eq. (3)} && \forall\, t \in [t_0, t_{i+1}], && \text{(19b)}\\
&\mathbf{x}(t_0) = \mathbf{x}_0, && && \text{(19c)}\\
&\Pr[\mathbf{x}(t) \in \mathcal{X}] \ge 1 - \varepsilon_s && \forall\, t \in [t_0, t_{i+1}], && \text{(19d)}\\
&\Delta\mathbf{v}_i \in \mathcal{U}, && && \text{(19e)}\\
&\Pr[\mathbf{r}(t_k) \in \mathcal{R}_f] \ge 1 - \varepsilon_f && \forall\, f \in \mathcal{F}_g,\ \text{for } t_k \in [t_0, t_{i+1}]. && \text{(19f)}
\end{aligned}
$$

where ε_s and ε_s are risks associated with the desired probabilistic satisfaction of the relative constraints. The implementation details for Eq. (19) are provided Subsection 4.2.

In the refinement stage, the planning horizon times and the times associated with the scientific constraints are fixed; the time spent in the ROIs is not optimized. This step focuses on guaranteeing robustness with respect to uncertainties and reducing fuel consumption, which is considered an additional relevant aspect. If stricter requirements apply, different trajectory refinement objective functions can be considered. The choice of splitting the problem into two subproblems aims at enhancing computational efficiency: the trajectory generation performs a rapid exploration to identify regions of the control set with high scientific return, and the subsequent refinement steps enforce robustness in a lower-dimensional space. This dimensionality reduction enhances convergence properties and computational time, at the expense of optimality.

4. Methodology

In this section, the approaches used to solve the problems stated in Section 3 are described in detail. The sec-

Copyright ©2025 by Alban Beshaj. Published by the IAF, with permission and released to the IAF to publish in all forms.

Algorithm 1: Sampling-based scheme

Input: initial samples n_0, max iterations n_{it}, best samples n_{best}, refinement samples n_{ref}
Output: best impulse $\mathbf{\Delta v}^*$ and score $T_{f,\mathrm{tot}}(\mathbf{\Delta v}^*)$
(1) Initial sampling:
$U^{(0)} \leftarrow \textsc{InitialSampling}(n_0)$;
for $k = 0, \ldots, n_{\mathrm{it}}$ **do**
  (2) Forward propagate: **for all** $\mathbf{\Delta v} \in U^{(k)}$
  $\mathrm{traj}(\mathbf{\Delta v}) \leftarrow \textsc{ForwardPropagate}(\mathbf{\Delta v})$;
  (3) Evaluate objective: **for all** $\mathbf{\Delta v} \in U^{(k)}$
  $T_{f,\mathrm{tot}}(\mathbf{\Delta v}) \leftarrow \textsc{Evaluate}(\mathrm{traj}(\mathbf{\Delta v}))$;
  (4) Select most promising:
  $S^{(k)} \leftarrow \textsc{SelectBest}(U^{(k)}, T_{f,\mathrm{tot}}, n_{\mathrm{best}})$;
  if $k = n_{\mathrm{it}}$ **then**
    break
  (5) Refine mesh:
  $U^{(k+1)} \leftarrow \textsc{RefineMesh}(S^{(k)}, n_{\mathrm{ref}})$;

tion starts by presenting the trajectory generation method, which is based on a sampling-based scheme that is efficiently initialized. It proceeds by providing the details of the trajectory refinement approach, which solves a convex problem to obtain robust fuel-optimal solutions.

4.1 Trajectory generation problem

The trajectory generation problem, as stated in Section 3, involves finding a control action that maximizes the scientific return within the considered planning horizon. This problem can be particularly complex in the presence of a large number of ROIs, as the objective function becomes very irregular, compromising the reliability of gradient-based methods. To enhance robustness of the trajectory generation process, this work uses a sampling-based approach, a technique widely used in other fields [17, 18]. Following previous works that have applied this technique in the context of goal-oriented guidance [7, 8], the method used in this study evaluates the reachable sets resulting from the samples taken in the control space. While under simpler dynamics, the control execution time can be included as a decision variable with a limited impact on the algorithm computational demand [16, 19], the complexity of close-proximity dynamics around minor bodies precludes this choice.

Similar to [8], the optimal impulse search is based on Algorithm 1. In brief, the algorithm iterates over the generation of a set of control actions, which are forward propagated and scored by the objective $T_{f,\mathrm{tot}}$. In each iteration, a mesh refinement is performed around the most promising samples. The control domain sampling is performed using a Fibonacci distribution [20], to guarantee approximately uniform coverage. The radius of the initial mesh is determined by the control set requirement; the refinement mesh radius is equal to the minimum distance of the most promising sample from the already explored samples.

The main limitation of sampling-based methods is their sensitivity to the number and placement of initial samples. Indeed, the information used in the refinement process is mainly based on the initial samples. Although this aspect can be mitigated through advanced sampling techniques, the refinement still relies on the initial scoring, and this can lead to poor performance of the method on highly irregular objective functions. To enhance the stability of the method, this work proposes an informed initialization, rather than a uniform first sampling, to start the refinement directly from the most promising regions of the control set.

In order to efficiently locate regions of the control space with high scientific return, the simple Keplerian dynamics is exploited. Specifically, a set of Lambert problems is solved to find the impulses that connect the initial state $\mathbf{x}_0$ to points on normals of each $\mathcal{R}_f$ over a grid of arrival times that satisfy the incidence angle condition in Eq. (1c) for that feature. This produces a finite set of candidate control impulses:

$$\mathcal{U}_L = \{\, \mathbf{\Delta v}_{f,k,i} \in \mathbb{R}^3 :\ f \in \mathcal{F},\ k \in \{1, \ldots, K_f\}, \quad t_i \in \mathcal{T}_f \,\}. \qquad (20)$$

where k is the index identifying the axial sample on $\mathcal{R}_\{$ (ignoring the incidence angle condition), and t_i is the arrival time of the set $\mathcal{T}_f$ representing the arrival times in $[t_i,\ t_{i+1}]$ for which the incidence angle condition holds.

The impulses in $\mathcal{U}_L$ are then clustered in spherical coordinates space. Two or more control actions are considered compatible if the differences in magnitude, azimuth, and elevation angles are below prescribed thresholds. Once clusters of compatible impulses are identified, they are ranked according to the number of $\mathcal{R}_f$ that they intersect, and to an approximate cumulative time spent within those ROIs. The consideration of the first criterion is justified by the cost of Eq. (17), while the second enhances the robustness with respect to uncertainties, a crucial aspect for the trajectory refinement process. The two criteria are weighted equally in the ranking process.

In addition to the initial seed generation, the same methodology is also applied to identify promising maneuver times. Using a small set of samples in the initial mesh significantly reduces the time required for its evaluation. This gain in computational efficiency allows for the inclusion of the time domain in the search space of the

Copyright ©2025 by Alban Beshaj. Published by the IAF, with permission and released to the IAF to publish in all forms.

sampling-based methodology.

However, non-Keplerian propagation remains expensive and limits the temporal discretization. Leveraging on the observed correlation between the results obtained applying Algorithm 1 under Keplerian and non-Keplerian dynamics (see Figure 7), the sampling-based search for the maneuver time is performed using the Kepler analytical solution in the forward propagate step. The computational efficiency of the two-body dynamics propagation permits a finer grid in $[t_{i+1},\ t_{i+1}+\Delta T_m]$, enabling the selection of subsequent maneuver epochs with high scientific return, thus reducing the greedy nature of the approach used.

4.2 Trajectory refinement problem

The trajectory refinement problem formalized in Section 3 is solved through a direct approach, chosen for the favorable convergence properties [21], an aspect fundamental for the approach presented in this study, as the initial guess is provided from a different optimization problem and can have poor robustness characteristics. The continuous-time problem in Eq. (19) is discretized in a finite number of nodes N, containing the maneuver time t_i and the times t_k associated with the passage through the ROIs in $\mathcal{F}_g$. Among direct approaches, a convex formulation is adopted to exploit the efficiency offered by convex solvers [22]. In particular, the Sequential Convex Programming (SCP) algorithm is selected, a method demonstrated to be effective for low-trust interplanetary transfer missions [23, 24], powered descent and landing [25, 26], and rendezvous and proximity operations applications [27].

In order to be able to solve the problem stated in Subsection 4.2 through the SCP, the refinement problem must be reformulated. Specifically, the SCP admits a convex objective function, affine equality constraints and inequality constraints defining convex sets [28]. The problem in Eq. (19) does not satisfy the required conditions. In particular, Eq. (3) is a non-linear equality constraint, and Eqs. (19d) and (19f) represent probabilistic constraints that must be converted in tractable constraints. Starting from the non-linear dynamics, it is transformed into an affine equality constraint by linearization. Considering $\hat{\mathbf{x}}$ and $\boldsymbol{\Delta}\hat{\mathbf{v}}$ as the nominal trajectory and the nominal control action, the motion around it can be described by the linear relation in Eq. (7). The chance constraints require additional considerations to be reformulated. First of all, the set $\mathcal{X}$ defined in Eq. (15) represents a hollow sphere, which is not convex. The set $\mathcal{R}_f$ instead can assume complex shapes described by Eq. (2) due to its time dependence on the incidence angle. However, in case all points satisfy the three conditions in Eq. (2), $\mathcal{R}_f$ can be approximated by a truncated Second Order Cone (SOC), which is a convex set.

The geometrical considerations above are not sufficient to transform the chance constraint into a convex constraint, and additional considerations are required. Following [29], in case a generic feasible set is affine ($\mathcal{S} = \{\, \mathbf{x} \mid \mathbf{h}^\top \mathbf{x} + b \le 0 \,\}$) and the constrained variable $\mathbf{x}$ is described by a Gaussian distribution $\mathcal{N}(\bar{\mathbf{x}}, P_x)$, the chance constraint $Pr[x \in \mathcal{S}] \ge 1-\varepsilon$ is equivalent to the following linear inequality:

$$\mathbf{h}^\top \bar{\mathbf{x}} + b + \Psi(1-\varepsilon)\sqrt{\mathbf{h}^\top P_x\,\mathbf{h}} \le 0 \tag{21}$$

where $\Psi(\cdot)$ is the inverse of the Gaussian cumulative distribution function. Note that once a risk level ε is selected, $\Psi(1-\varepsilon)$ becomes a scalar value.

Given that the state distribution is considered Gaussian, transforming Eqs. (19d) and (19f) into the linear form in Eq. (21) requires only an affine representation of the sets $\mathcal{X}$ and $\mathcal{R}_f$. The non-convex set $\mathcal{X}$ is locally approximated, at the node j, by two bounding half-spaces: the impact and the escape planes. The two bounds are imposed as:

$$\underbrace{-\frac{\hat{\mathbf{r}}_j^\top}{\|\hat{\mathbf{r}}_j\|}}_{\mathbf{h}_\mathrm{i}}\mathbf{r}_j + \underbrace{R_{imp}}_{b_i} \le 0, \tag{22a}$$

$$\mathbf{h}_\mathrm{s}{}^\top \mathbf{r}_j \ \underbrace{-R_{esc}}_{b_s} \le 0, \qquad s = 1,\ldots,N_{esc}. \tag{22b}$$

where N_{esc} is the number of planes used to approximate the escape condition, and $\mathbf{h}_\mathrm{s}$ are the associated normals. These planes can be generated to cover a prescribed angular sector of the escape sphere. Note that while the affine formulation of the impact constraint is conservative, the one associated with the escape is not; therefore, to increase the fidelity of the affine representation of the escaping requirement, a higher number of N_{esc} is required.

Analogously, the truncated SOCs representing the ROIs can be approximated using a set of bounding lateral planes plus two bounding planes with the normals aligned with $\pm\mathbf{n}_\mathrm{f}$. Defining an angular variable $\phi_\ell = \dfrac{2\pi(\ell-1)}{N_\ell} + \phi_0$ with $\ell = 1,\ldots,N_\ell$ where N_ℓ is the number of approximating lateral planes, the ℓ-th lateral plane normal is:

$$\mathbf{h}_\ell = \cos\epsilon_{\max}\big(\cos\phi_\ell\,\mathbf{e}_1 + \sin\phi_\ell\,\mathbf{e}_2\big) - \sin\epsilon_{\max}\,\mathbf{n}_f \tag{23}$$

where $\mathbf{e}_1$ and $\mathbf{e}_2$ are an orthonormal pair on the plane defined by $\mathbf{n}_\mathrm{f}$. In this work, $\mathbf{e}_1$ is aligned with the vector $\mathbf{p}_1 - (\mathbf{p}_1{}^\top\mathbf{n}_\mathrm{f})\,\mathbf{n}_\mathrm{f}$, where $\mathbf{p}_1$ is the principal direction associated

Copyright ©2025 by Alban Beshaj. Published by the IAF, with permission and released to the IAF to publish in all forms.

with the maximum eigenvalue of P_{rr}. This choice reduces the conservative nature of the deterministic representation of the SOCs chance constraint.

In addition to the lateral planes, two other planes are added for the range bounds associated with the ROI. The complete affine representation of the truncated SOC is:

$$\underbrace{\begin{bmatrix} \mathbf{h}_1^\top \\ \vdots \\ \mathbf{h}_{N_l}^\top \\ -\mathbf{n}_f^\top \\ \mathbf{n}_f^\top \end{bmatrix}}_{H} \mathbf{r}_\mathbf{j} + \underbrace{\begin{bmatrix} -\mathbf{h}_1^\top \mathbf{r}_f \\ \vdots \\ -\mathbf{h}_{N_l}^\top \mathbf{r}_f \\ \mathbf{n}_f^\top \mathbf{r}_f + \rho^- \\ -\mathbf{n}_f^\top \mathbf{r}_f - \rho^+ \end{bmatrix}}_{b} \leq \mathbf{0}. \tag{24}$$

All the previous vectors are expressed in the frame $\mathcal{I}$; the frame superscript is omitted to simplify the notation.

Given the affine representation of all constraints, the last step is to manage the assignment of the probability risk for the sets approximated by multiple affine functions. This probability allocation problem is conservatively solved using Boole's inequality. The single chance constraint imposed on a set defined by the intersection of N_s affine sets:

$$\Pr\left[\bigcap_{i=1}^{N_s} x \in S_i\right] \geq 1 - \varepsilon \tag{25}$$

can be transformed into N_s chance constraints, one for each set:

$$\bigcap_{i=1}^{N_s} \Pr[x \in S_i] \geq 1 - \varepsilon_i \;\; \text{with} \;\; \sum_{i=1}^{N_s} \varepsilon_i \leq \varepsilon \tag{26}$$

The choice of the single ε_i can be dictated by considerations associated with the specific problem. However, in this work, a uniform risk allocation is considered. Moreover, since a conjunction of affine sets approximates all the constraints, all approximating planes must be considered in the risk allocation [30].

Given the considerations above, the problem stated in Eq. (19) can be reformulated as the convex problem reported in Eq. (27), where $\boldsymbol{\Delta}\mathbf{v}_i = \boldsymbol{\Delta}\hat{\mathbf{v}}_i + \boldsymbol{\delta}\mathbf{v}_\mathrm{i}$, $\boldsymbol{\nu}_j = \boldsymbol{\nu}(t_j)$ are slack variables to avoid artificial infeasibility, and Eq. (27h) represents the trust region constraint. R is the trust region radius, which is managed through the simple hard trust region with constant rates approach [31]:

$$R^{(n+1)} = \begin{cases} \dfrac{R^{(n)}}{\alpha}, & \rho_0 \leq \rho^{(n)} < \rho_1, \\ R^{(n)}, & \rho_1 \leq \rho^{(n)} < \rho_2, \\ \beta R^{(n)}, & \rho^{(n)} \geq \rho_2. \end{cases} \tag{28}$$

If $\rho \leq \rho_0$ the solution is rejected. In Eq. (28) n denotes the iteration number of the SCP; ρ_0, ρ_1, ρ_2, α, and β are constant parameters determining the trust region contraction and expansion. Moreover, the quantity $\rho^{(n)}$, defined as the ratio between the actual cost decrease and the predicted cost decrease, determines if the n-th solution of the convex optimization is accepted or rejected [28].

Convergence of the SCP is based on two quantities: the linear constraint violation and the normalized difference in the objective between two consecutive iterations. The algorithm terminates when these quantities fall below ε_L (linear constraint violation tolerance) and ε_J (objective tolerance), respectively. The problem in Eq. (27) is solved in MATLAB through CVX [32, 33] modeling framework and gurobi solver [34].

5. Results

The numerical testing of the developed methodology is performed considering a mission to the asteroid Itokawa. In this section, the main parameters defining the scenario and the algorithmic settings required are provided. Results are presented both for the single algorithms and for the complete methodology.

5.1 Scenario definition

The dynamic environment includes the forces described in Subsection 2.1. Specifically, the central and non-spherical contributions of the minor body gravity field, the SRP, and the gravitational attraction of the Sun are considered. The set $\mathcal{F}$ is composed of 14 features randomly chosen on the surface of the body model, which are represented in Figure 2, neglecting their dependence on the incidence angle. All the main simulation parameters that define the dynamics around Itokawa, the ROIs, and the considered uncertainties are reported in Table 1. The initial conditions of the simulations are taken from a Sun-Stabilized Terminator Orbit (SSTO) obtained with the algorithm described in [35], with semimajor axis $a_0 = 1.5$ km. Initial epochs t_0 are evenly spaced over almost three orbital periods, using 2nd November 2002 as the initial reference epoch t_ref. Two reference frames are used. The frame $\mathcal{B}$, a non-inertial reference frame with the z-axis aligned with the rotational axis of Itokawa, the x-axis aligned with the prime meridian of the asteroid, and the y-axis completing the right-hand frame. The frame $\mathcal{I}$ is the inertial frame ECLIPJ2000 centered on the barycenter of the minor body.

Copyright ©2025 by Alban Beshaj. Published by the IAF, with permission and released to the IAF to publish in all forms.

$$\underset{\Delta \mathbf{v}_i}{\text{minimize}} \quad \|\Delta \mathbf{v}_i\| + \sum_{j=1}^{N} \lambda \|\boldsymbol{\nu}_j\|_1 \tag{27a}$$

subject to

$$\delta \mathbf{x}_{j+1} = \Phi(t_{j+1}, t_j)\delta \mathbf{x}_j + \Phi(t_{j+1}, t_j) B\, \delta \mathbf{v}_j + \boldsymbol{\nu}_j \qquad \text{for } j = 0, \dots, N, \tag{27b}$$

$$\mathbf{x}(t_0) = \mathbf{x}_0, \tag{27c}$$

$$\|\Delta \mathbf{v}_i\| \leq \Delta v_{\max}, \tag{27d}$$

$$\mathbf{h}_i^\top \bar{\mathbf{r}}_j + b_i + \Psi(1 - \varepsilon_s)\sqrt{\mathbf{h}_i^\top P_{rr,j}\, \mathbf{h}_i} \leq 0 \qquad \text{for } j = 0, \dots, N, \tag{27e}$$

$$\mathbf{h}_{j,s}^\top \bar{\mathbf{r}}_j + b_{j,s} + \Psi\left(1 - \frac{\varepsilon_s}{N_{esc}}\right)\sqrt{\mathbf{h}_{j,s}^\top P_{rr,j}\, \mathbf{h}_{j,s}} \leq 0 \qquad \text{for } s = 1, \dots, N_{esc}, \text{ for } j = 0, \dots, N, \tag{27f}$$

$$\mathbf{h}_{f,\ell}^\top \bar{\mathbf{r}}_k + b_{f,\ell} + \Psi\left(1 - \frac{\varepsilon_f}{N_\ell + 2}\right)\sqrt{\mathbf{h}_{f,\ell}^\top P_{rr,k}\, \mathbf{h}_{f,\ell}} \leq 0 \qquad \forall f \in \mathcal{F}_g, \text{ for } \ell = 1, \dots, N_\ell{+}2, \text{ for } t_k \in \{t_0, \dots, t_N\}, \tag{27g}$$

$$\|\delta \mathbf{x}_j\|_1 \leq R \qquad \text{for } j = 0, \dots, N. \tag{27h}$$

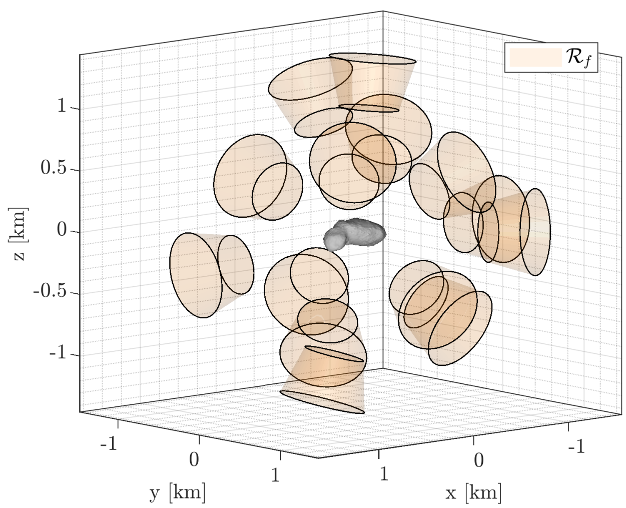

Fig. 2: Representation of ROIs in the frame $\mathcal{B}$, neglecting incidence angle dependence.

Table 1: Scenario parameters.

	Parameter	Value
Spacecraft	a_0	1.5 km
	m	20 kg
	C_r	1.21
	A	$1\ \mathrm{m}^2$
Main body	Gravity type	Spherical harmonics
	μ	$2.36 \times 10^{-9}\ \mathrm{km}^3/\mathrm{s}^2$
	Order and degree	4×4 [36]
	T	12.1324 h [37]
ROIs	(ρ_f^-, ρ_f^+)	(0.9 km, 1.3 km)
	$(\epsilon_f^-, \epsilon_f^+)$	(0°, 15°)
	(i_f^-, i_f^+)	(0°, 90°)
Uncertainty	(σ_r, σ_v)	(50 m, 1 mm/s)
	(σ_m, σ_p)	(3%, 3°)

5.2 Sampling-based trajectory generation

The trajectory generation methodology described in Section 4 is tested considering a subset of the initial conditions used for the testing of the complete methodology. Specifically, the analyses reported below consider the first 100 of the total 200 samples taken from the initial SSTO. The parameters used by the sampling-based algorithm are reported in Table 2. The parameters associated with the engineering constraints are the same as those used also for the trajectory refinement. In Figure 3, the performances of the methodology in terms of total time spent inside ROIs are reported for the initial conditions considered. To compare the classical sampling strategy with the Lambert-based initialization, results for both methods are shown. It can be noted that in most cases, the Lambert-informed sampling outperforms the classical one. Specifically, considering all the simulations performed, the Lambert initialization allows for an increase in $T_{f,\text{tot}}$ of approximately 10% with a decrease in computational cost of about 50%. This computational gain reflects the smaller number of initial samples used, capped at 20 for the Lambert initialization and equal to 350 for the classical scheme.

Copyright ©2025 by Alban Beshaj. Published by the IAF, with permission and released to the IAF to publish in all forms.

Table 2: Sampling-based parameters.

Parameter	Value
K_1, K_2, K_3, $\bar{R}$	(10, 100, 100, 1 km)
Δv_{max}	0.1 m/s
ΔT_m, ΔT_p)	(18.5 h, 4 h)
(R_{imp}, R_{esc})	(0.7 km, 3 km)
(n_0, n_{it}, n_{best}, n_{ref})	(350, 3, 6, 18)

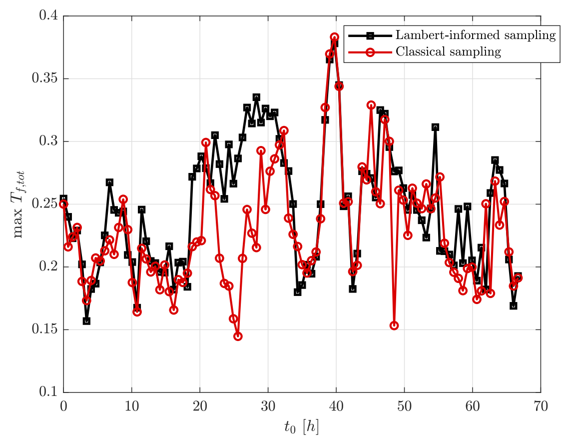

Fig. 3: Comparison of maximum objective value for different initial conditions using classical and Lambert-informed sampling.

The effectiveness of the clustering in identifying promising regions of the control set can also be seen in Figure 6, where the score of the single impulse is reported for a dense sampling of the control domain. The Lambert seeds, along with their associated search radius, cover the control regions with higher scores. Note that in Figure 6 all the solutions resulting from the clustering are reported; however, as reported previously, only the top 20 seeds in the ranking are used as initial samples.

The results shown in Figure 3 are obtained with n_0 = 350. Given the high relevance of this parameter, additional analyses are conducted to assess its influence on the performance of the methodology. In Figures 4 and 5, the maximum $T_{f,\text{tot}}$ obtained with a varying n_0 for the classical sampling and the one obtained with the Lambert initialization are presented for two initial conditions considered in the previous analysis, which will be referred to as Gen1 and Gen2.

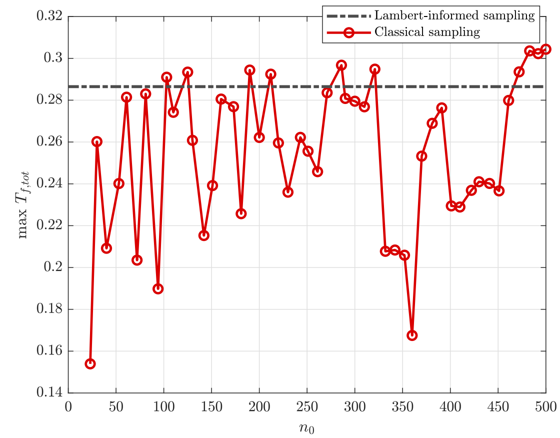

Fig. 4: Maximum objective value for classical sampling with varying initial samples, and for Lambert-informed sampling (Gen1)

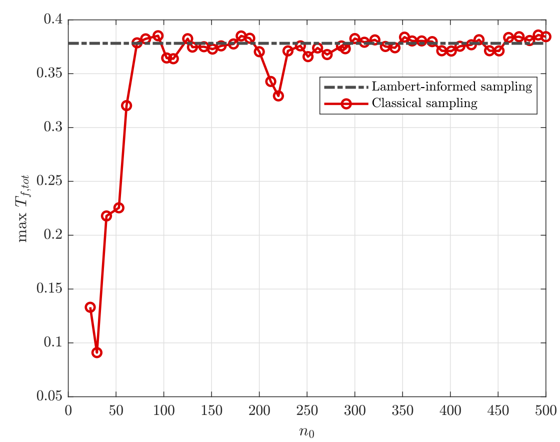

Fig. 5: Maximum objective value for classical sampling with varying initial samples, and for Lambert-informed sampling (Gen2).

The case Gen1 is associated with an irregular objective function, as reflected from the irregular trend of $T_{f,\text{tot}}$ for increasing n_0. On the other hand, Gen2 is associated with a more regular objective function, at least near the minimum. In this case, the value of the maximum found initially rises and then plateaus, indicating stable performance of the sampling-based methodology. In both cases, the benefit of initializing the scheme with the Lambert seeds is evident. Regardless of the objective function regularity, the maximum found with the Lambert-informed sampling is close to the highest one obtained by the classical sampling.

Copyright ©2025 by Alban Beshaj. Published by the IAF, with permission and released to the IAF to publish in all forms.

Moreover, it is worth mentioning that the value of the maximum associated with the Lambert-informed sampling is obtained with a maximum $n_0 = 20$, which corresponds to the minimum number of initial samples n_0 for the classical sampling reported in Figures 4 and 5; refinement parameters are the same for both methods.

Figure 7 reports the difference in the maximum scientific return applying the Lambert-informed sampling under non-Keplerian and Keplerian dynamics for the same initial conditions considered in the analysis in Figure 3. A strong correlation between the two results can be observed. In most cases, the differences are related to the intrinsic variability of the sampling-based strategy. In fewer cases, the optimal impulse completely changes under full dynamics; yet, trajectories close to those resulting from optimal Keplerian impulses still yield high objective values under non-Keplerian dynamics. For these reasons, the developed methodology explores the time domain with multiple sampling in the control domain for different initial times and initial states along the flown arc. Then it selects the maneuver time at Keplerian peaks of $T_{f,\mathrm{tot}}$.

5.3 SCP-based trajectory refinement

As indicated in Subsection 3.3, the convex-based trajectory refinement optimization is performed for each planned arc, using the solution of the trajectory generation problem as the initial guess. The main parameters required by the SCP are reported in Table 3. Two representative cases are shown in Figures 8 and 10 (Ref1 and Ref2). The corresponding trends of normalized fuel consumption are reported in Figures 9 and 11. The results of these cases are reported as they are representative of the behaviors shown by the trajectory refinement process. The case Ref1 represents an arc that crosses a small number of ROIs. When the trajectory generation provides an arc with similar properties, the refinement can move more with respect to the first guess, achieving a high reduction of the fuel consumption (see Figure 9). The case Ref2 is characterized by the crossing of a high number of ROIs. Usually, in this case, the tighter feasibility envelope constrains the optimizer, limiting the reduction in fuel consumption, and it increases the number of rejected solutions (Figure 11).

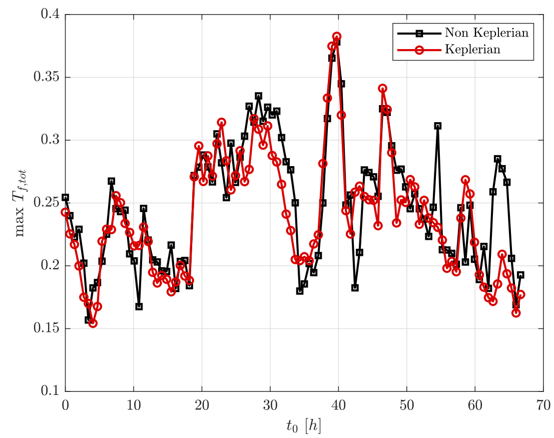

Fig. 7: Comparison between the maximum $T_{f,tot}$ obtained for an arc under non-Keplerian and Keplerian dynamics through the sampling-based trajectory generation. Each point represents an initial condition on the initial SSTO.

In addition to the two cases reported above, there is a third condition that interferes more with the proper refinement of the solution. This case is associated with the grazing of specific ROIs or with incompatibilities between ROIs, which renders the optimization problem ill-posed. These cases are handled by solving a simple convex feasibility problem, which provides the ROI set to exclude, thereby recovering a well-posed problem. The resulting new problem typically reduces to one of the cases reported above.

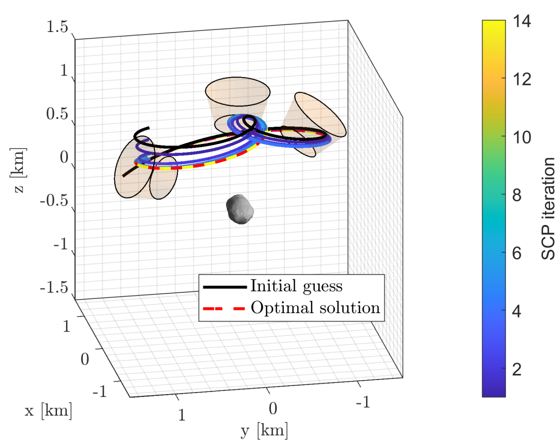

Fig. 8: Trajectory evolution in frame $\mathcal{B}$ for case Ref1 showing the initial guess, the SCP accepted iterations, and the optimal solution.

Copyright ©2025 by Alban Beshaj. Published by the IAF, with permission and released to the IAF to publish in all forms.

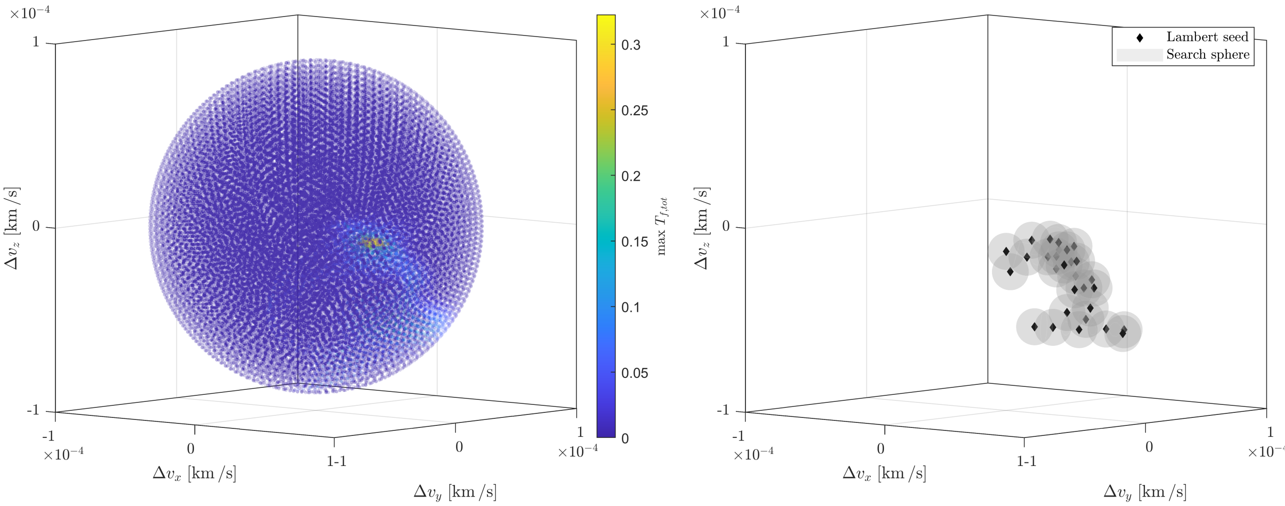

Fig. 6: Control set score for 5000 samples (left); seeds and associated search sphere identified by Lambert clustering as high scientific return regions (right).

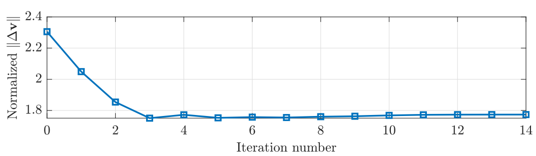

Fig. 9: Trend of $\mathbf{\Delta v}$ magnitude over SCP iterations for case Ref1.

Table 3: SCP parameters

Parameter	Value
λ	100
R_0	5
$(\rho_0,\ \rho_1,\ \rho_2)$	$(0.01,\ 0.2,\ 0.85)$
$(\alpha,\ \beta)$	$(1.5,\ 1.5)$
$(\varepsilon_s,\ \varepsilon_f)$	$(10^{-4},\ 0.2)$
$(\varepsilon_J,\ \varepsilon_L)$	$(10^{-4},\ 10^{-6})$

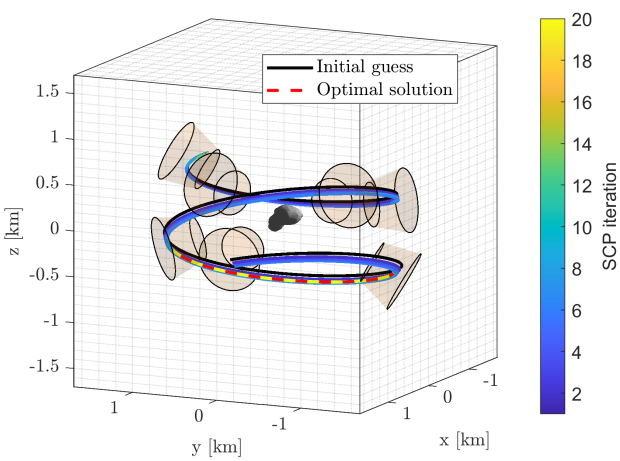

Fig. 10: Trajectory evolution in frame $\mathcal{B}$ for case Ref2 showing the initial guess, the SCP accepted iterations, and the optimal solution.

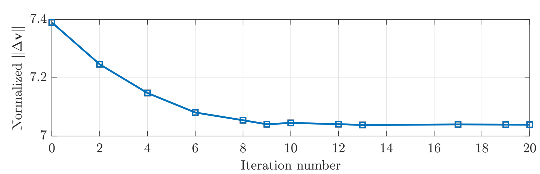

Fig. 11: Trend of $\mathbf{\Delta v}$ magnitude over SCP iterations for case Ref2.

5.4 Two-step guidance

The complete methodology, which combines Lambert-informed sampling-based trajectory generation and convex trajectory refinement, is tested through Monte Carlo (MC) simulations using 200 initial conditions generated as described in Subsection 5.1. In Figures 12 and 13, the statistics of the total time and the total Δv required to satisfy all the scientific requirements are reported. With the 14 features represented in Figure 2, the stochastic Δv required

Copyright ©2025 by Alban Beshaj. Published by the IAF, with permission and released to the IAF to publish in all forms.

to complete the mission is 0.59 m/s and the stochastic t_f is 140.5 h, both estimated as the $99th$ percentile of the associated CDF. For comparizon, the same results are reported in Figures 14 and 15 using the sampling-based trajectory generation, without the refinement step. The generation step alone can complete the whole mission, but with slightly worse performance. In this case, the stochastic Δv and t_f are respectively 0.76 m/s and 147.2 h, which correspond to an increase of about 22% in fuel consumption and 5% in the total time required to complete the mission. Note that satisfactory results can also be obtained with the single generation step, as maximizing the time spent in the ROIs enhances the robustness of the solution.

The results reported in this section are strongly correlated with the dynamical environment of the asteroid. Therefore, they are indicative of a minor body with a main gravity similar to that of Itokawa. For more massive bodies, both Δv and t_f can increase considerably due to the reduced state space connectivity. Figures 16 and 17 report one of the trajectories obtained from the MC simulations in the frames $\mathcal{B}$ and $\mathcal{I}$. To simplify the representation, in the frame $\mathcal{B}$ the ROIs are represented as truncated SOCs, ignoring their dependence on incidence angle, while in frame $\mathcal{I}$ only the ROIs entry points are reported, since the regions are not static in this frame.

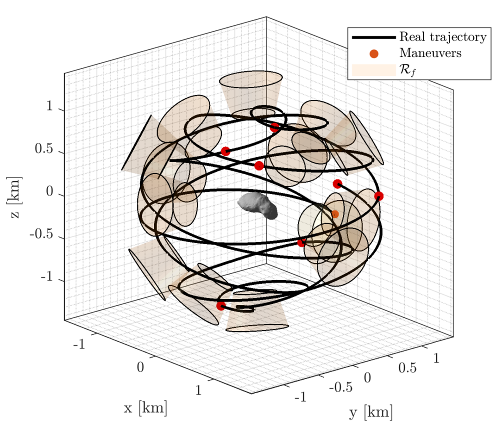

Fig. 16: Real trajectory evolution in frame $\mathcal{B}$ for one MC sample, with ROIs shown as truncated SOCs and maneuvers represented as red dots.

In the cases considered, all ROIs are visited at least once by the actual trajectory, as the simulation is stopped only when all $\mathcal{R}_f$ are satisfied. In Figure 18, the evolution of the ROIs satisfaction is reported for each MC sample. It can be noted that the distribution of the first ROIs satisfaction describes a right-skewed distribution, which gradually shifts toward a more symmetric distribution for the final ROIs satisfaction. This phenomenon could be related to the greedy nature of the approach used to solve the problem in Eq. (17), combined with the presence of a higher number of ROIs in the first part of the simulation.

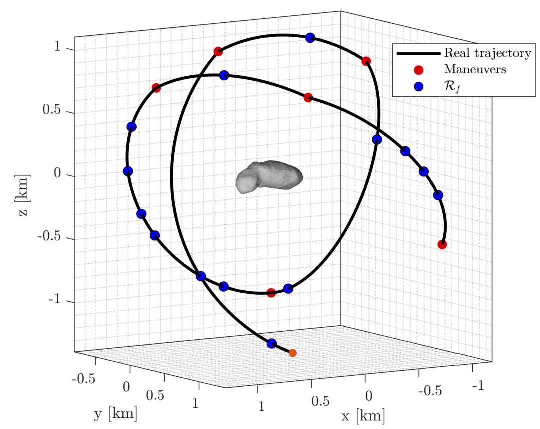

Fig. 17: Real trajectory evolution in frame $\mathcal{I}$ for one MC sample, with ROIs shown as blue dots and maneuvers represented as red dots.

6. Conclusions

In this work, a two-step guidance methodology for close-proximity operations around asteroids is proposed. The developed guidance algorithm enables the spacecraft to satisfy both typical engineering constraints and scientific requirements associated with observing specific regions of the minor body surface. Although numerical testing is conducted under a scenario involving a spacecraft equipped with a passive sensor, the flexibility of the methodology allows for its application to other instruments, assuming that their requirements permit a geometrical representation in the state space.

The first step of the methodology solves a deterministic optimization through an efficient sampling-based algorithm, which is initialized by exploiting a clustering of Lambert solutions. The trajectory generated with the first stage is then used as an initial guess for a convex-based optimization, which refines the solution to enhance robustness with respect to uncertainties and minimize fuel consumption. The results obtained from the numerical testing demonstrate the capability of the methodology in mapping specific regions on the minor body surface. While the first step alone can satisfy mapping requirements, improved re-

Copyright ©2025 by Alban Beshaj. Published by the IAF, with permission and released to the IAF to publish in all forms.

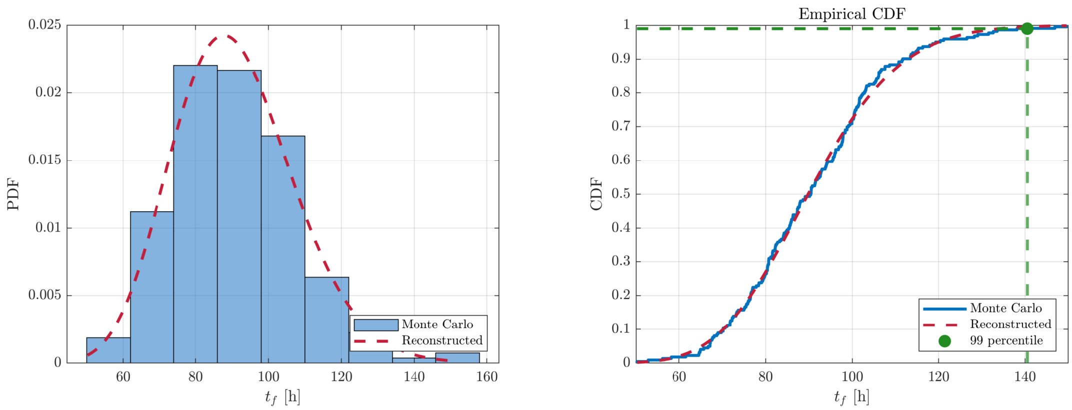

Fig. 12: Time required to satisfy all scientific requirements with two-step guidance. On the left probability distribution function. On the right cumulative distribution function.

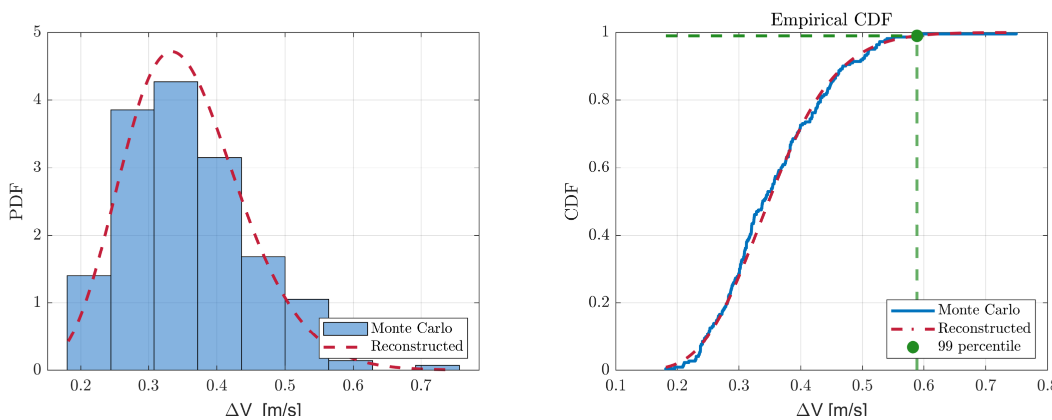

Fig. 13: **Δv** required to satisfy all scientific requirements with two-step guidance. On the left probability distribution function. On the right cumulative distribution function.

sults are achieved when the complete method is applied. Overall, the proposed approach represents a step toward autonomous close-proximity operations around minor bodies, enabling science-driven missions that are required to unlock the full potential of this class of targets.

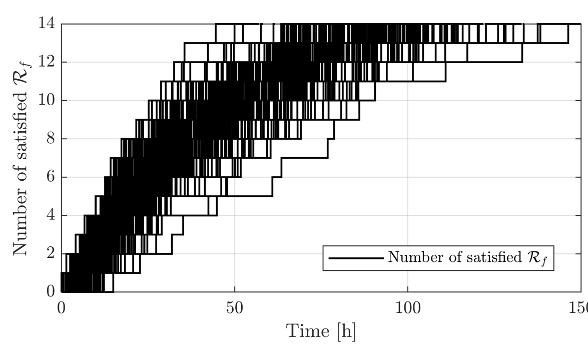

Fig. 18: Evolution of ROIs satisfaction for each MC sample.

Copyright ©2025 by Alban Beshaj. Published by the IAF, with permission and released to the IAF to publish in all forms.

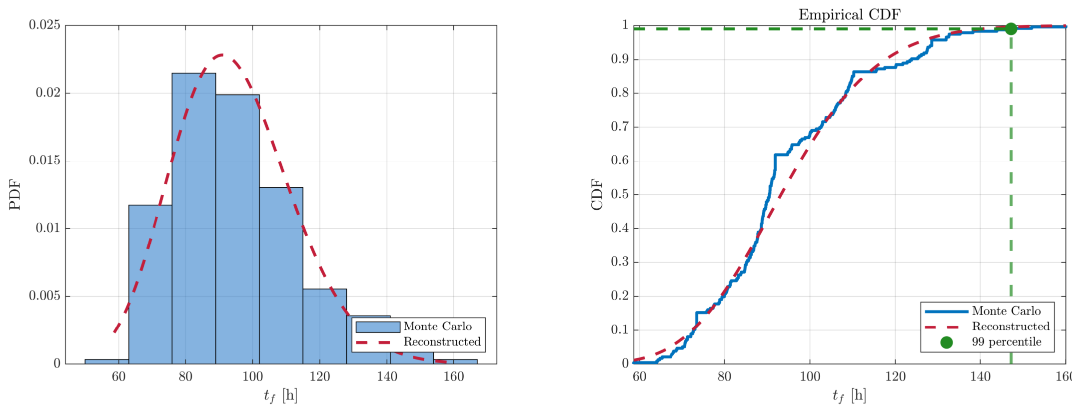

Fig. 14: Time required to satisfy all scientific requirements with sampling-based methodology. On the left probability distribution function. On the right cumulative distribution function.

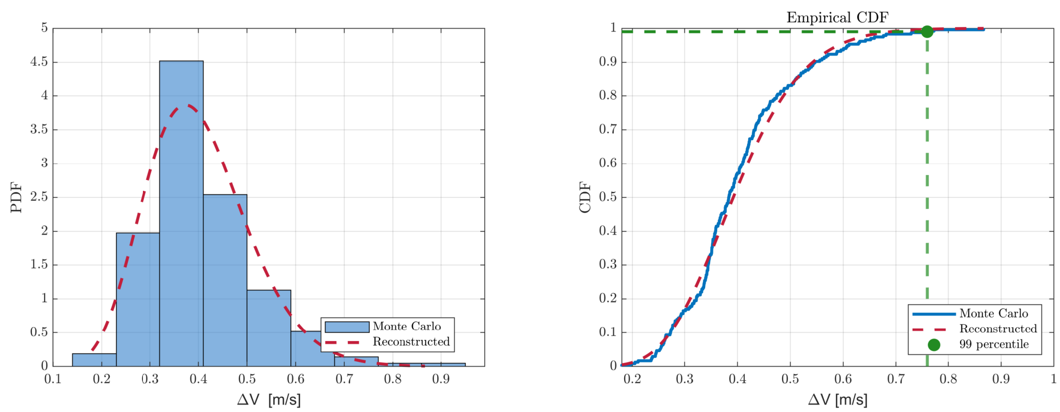

Fig. 15: Δv required to satisfy all scientific requirements with sampling-based methodology. On the left probability distribution function. On the right cumulative distribution function.

Acknowledgements

A.B. and F.T. acknowledge the financial support offered by the European Union under the Next Generation EU program, Mission 4, Component 1 (CUP D43C23002190008), to support the PhD studies of A.B.. This work was partially carried out as part of CASTOR, a project that has received funding from the European Union's Horizon Europe research and innovation programme under the Marie Skłodowska-Curie grant agreement no. 101103826.

References

[1] M. Azadmanesh, J. Roshanian, and M. Hassanalian. On the importance of studying asteroids: A comprehensive review. *Progress in Aerospace Sciences*, 142:100957, 2023.

[2] D. J. Scheeres. *Orbital Motion in Strongly Perturbed Environments: Applications to Asteroid, Comet and Planetary Satellite Orbiters*. Springer Berlin Heidelberg, Berlin, Heidelberg, 2012.

[3] R. B. Negri, A. F. B. A. Prado, R. A. J. Chagas, and R. V. Moraes. Autonomous rapid exploration in close-proximity of asteroids. *Journal of Guidance, Control, and Dynamics*, 47(5):914–933, 2024.

[4] V. Pesce, A. Agha-mohammadi, and M. Lavagna. Autonomous navigation & mapping of small bodies. In *2018 IEEE Aerospace Conference*, pages 1–10, Big Sky, MT, March 2018. IEEE.

[5] M. Piccinin, P. Lunghi, and M. Lavagna. Deep Reinforcement Learning-based policy for autonomous imaging planning of small celestial bodies mapping.

Copyright ©2025 by Alban Beshaj. Published by the IAF, with permission and released to the IAF to publish in all forms.

Aerospace Science and Technology, 120:107224, 2022.

[6] A. Brandonisio, L. Capra, and M. Lavagna. Deep reinforcement learning spacecraft guidance with state uncertainty for autonomous shape reconstruction of uncooperative target. *Advances in Space Research*, 73(11):5741–5755, 2024.

[7] D. A. Surovik and D. J. Scheeres. Adaptive Reachability Analysis to Achieve Mission Objectives in Strongly Non-Keplerian Systems. *Journal of Guidance, Control, and Dynamics*, 38(3):468–477, March 2015.

[8] A. Rizza, C. Giordano, and F. Topputo. A goal-oriented guidance approach for binary asteroids exploration. *Astrodynamics*, 9(2):289–302, 2025.

[9] C. Giordano, S. Campagnola, and F. Topputo. Goal-oriented trajectories about minor bodies using sequential convex programming: a deterministic approach. In *35th AAS/AIAA Space Flight Mechanics Meeting*, pages 1–26, 2025.

[10] C. Giordano, S. Campagnola, and F. Topputo. Goal-oriented trajectories about minor bodies using sequential convex programming: a stochastic approach. In *35th AAS/AIAA Space Flight Mechanics Meeting*, pages 1–18, 2025.

[11] A. Rizza, S. D'Amico, and F. Topputo. Goal-Oriented Trajectory Refinement for Asteroid Mapping Using Sequential Convex Programming. *Journal of Guidance, Control, and Dynamics*, pages 1–15, August 2025.

[12] A. Rizza. *Goal-oriented guidance under uncertainties for small bodies exploration*. PhD thesis, 2024.

[13] D. A. Vallado. *Fundamentals of astrodynamics and applications*, volume 12. Springer Science & Business Media, 2001.

[14] Y. Luo and Z. Yang. A review of uncertainty propagation in orbital mechanics. *Progress in Aerospace Sciences*, 89:23–39, February 2017.

[15] C. R. Gates. A simplified model of midcourse maneuver execution errors. Technical Report 32-504, Jet Propulsion Laboratory, California Institute of Technology, Pasadena, CA, 1963.

[16] F. Capolupo and P. Labourdette. Receding-Horizon Trajectory Planning Algorithm for Passively Safe On-Orbit Inspection Missions. *Journal of Guidance, Control, and Dynamics*, 42(5):1023–1032, May 2019.

[17] D. D. Dunlap, E. G. Collins, and C. V. Caldwell. Sampling based model predictive control with application to autonomous vehicle guidance. In *Proceedings of the 2008 Florida Conference on Recent Advances in Robotics (FCRAR 2008)*, pages 1–6, Miami, FL, May 2008. Florida Institute of Technology.

[18] C. V. Caldwell, D. D. Dunlap, and E. G. Collins. Motion planning for an autonomous underwater vehicle via sampling based model predictive control. In *OCEANS 2010 MTS/IEEE SEATTLE*, pages 1–6, 2010.

[19] M. Maestrini and P. Di Lizia. Guidance Strategy for Autonomous Inspection of Unknown Non-Cooperative Resident Space Objects. *Journal of Guidance, Control, and Dynamics*, 45(6):1126–1136, June 2022.

[20] Á. González. Measurement of Areas on a Sphere Using Fibonacci and Latitude–Longitude Lattices. *Mathematical Geosciences*, 42(1):49–64, January 2010.

[21] J. T. Betts. Survey of Numerical Methods for Trajectory Optimization. *Journal of Guidance, Control, and Dynamics*, 21(2):193–207, March 1998.

[22] S. P. Boyd and L. Vandenberghe. *Convex optimization*. Cambridge University Press, Cambridge, UK ; New York, 2004.

[23] A. C. Morelli, C. Hofmann, and F. Topputo. Robust low-thrust trajectory optimization using convex programming and a homotopic approach. *IEEE Transactions on Aerospace and Electronic Systems*, 58(3):2103–2116, 2022.

[24] C. Hofmann and F. Topputo. Rapid Low-Thrust Trajectory Optimization in Deep Space Based on Convex Programming. *Journal of Guidance, Control, and Dynamics*, 44(7):1379–1388, July 2021. Publisher: American Institute of Aeronautics and Astronautics.

[25] B. Açıkmeşe and S. R. Ploen. Convex Programming Approach to Powered Descent Guidance for Mars Landing. *Journal of Guidance, Control, and Dynamics*, 30(5):1353–1366, September 2007. Publisher: American Institute of Aeronautics and Astronautics.

[26] M. Sagliano. Pseudospectral Convex Optimization for Powered Descent and Landing. *Journal of Guidance, Control, and Dynamics*, 41(2):320–334, February 2018. Publisher: American Institute of Aeronautics and Astronautics.

Copyright ©2025 by Alban Beshaj. Published by the IAF, with permission and released to the IAF to publish in all forms.

[27] T. Guffanti and S. D'Amico. Passively safe and robust multi-agent optimal control with application to distributed space systems. *Journal of Guidance, Control, and Dynamics*, 46(8):1448–1469, 2023.

[28] D. Malyuta, T. P. Reynolds, M. Szmuk, T. Lew, R. Bonalli, M. Pavone, and B. Açıkmeşe. Convex Optimization for Trajectory Generation: A Tutorial on Generating Dynamically Feasible Trajectories Reliably and Efficiently. *IEEE Control Systems*, 42(5):40–113, October 2022.

[29] K. Oguri and J. W. McMahon. Robust Spacecraft Guidance Around Small Bodies Under Uncertainty: Stochastic Optimal Control Approach. *Journal of Guidance, Control, and Dynamics*, 44(7):1295–1313, July 2021.

[30] K. Echigo, A. Cauligi, S. Bandyopadhyay, D. Scharf, G. Lantoine, B. Açıkmeşe, and I. Nesnas. Autonomy in the real-world: Autonomous trajectory planning for asteroid reconnaissance via stochastic optimization. In *AIAA SCITECH 2025 Forum*, page 1702, 2025.

[31] C. Hofmann, A. C. Morelli, and F. Topputo. On the Performance of Discretization and Trust-Region Methods for On-Board Convex Low-Thrust Trajectory Optimization. In *AIAA SCITECH 2022 Forum*, San Diego, CA & Virtual, January 2022. American Institute of Aeronautics and Astronautics.

[32] Inc. CVX Research. CVX: Matlab software for disciplined convex programming, version 2.2. https://cvxr.com/cvx, January 2020.

[33] M. Grant and S. Boyd. Graph implementations for nonsmooth convex programs. In V. Blondel, S. Boyd, and H. Kimura, editors, *Recent Advances in Learning and Control*, Lecture Notes in Control and Information Sciences, pages 95–110. Springer-Verlag Limited, 2008. http://stanford.edu/~boyd/graph_dcp.html.

[34] Gurobi Optimization, LLC. Gurobi Optimizer Reference Manual, 2024.

[35] S. Takahashi and D. J. Scheeres. Higher-Order Corrections for Frozen Terminator Orbit Design. *Journal of Guidance, Control, and Dynamics*, 43(9):1642–1655, September 2020.

[36] D. J. Scheeres, R Gaskell, S Abe, O Barnouin-Jha, T Hashimoto, J Kawaguchi, T Kubota, J Saito, M Yoshikawa, N Hirata, T Mukai, M Ishiguro, T Kominato, K Shirakawa, and M. Uo. The Actual Dynamical Environment About Itokawa. In *AIAA/AAS Astrodynamics Specialist Conference and Exhibit*, Keystone, Colorado, August 2006. American Institute of Aeronautics and Astronautics.

[37] A. Fujiwara, J. Kawaguchi, D. K. Yeomans, M. Abe, T. Mukai, T. Okada, J. Saito, H. Yano, M. Yoshikawa, D. J. Scheeres, O. Barnouin-Jha, A. F. Cheng, H. Demura, R. W. Gaskell, N. Hirata, H. Ikeda, T. Kominato, H. Miyamoto, A. M. Nakamura, R. Nakamura, S. Sasaki, and K. Uesugi. The rubble-pile asteroid itokawa as observed by hayabusa. *Science*, 312(5778):1330–1334, 2006.